Stateful characterization of resistive switching TiO$_2$ with electron beam induced currents

Running title: Stateful EBIC

Running Authors: Hoskins, *et al.*

Brian D. Hoskins [1,2,a], Gina C. Adam[3,4], Evgheni Strelcov[1,5],Nikolai Zhitenev[1], Andrei Kolmakov[1], Dmitri B. Strukov[3], Jabez J. McClelland[1]

[1)]Center for Nanoscale Science and Technology, National Institute of Standards and Technology, Gaithersburg, MD 20852, USA
[2)]Materials Department, University of California Santa Barbara, Santa Barbara, CA 93106, USA
[3)]Electrical and Computer Engineering Department, University of California Santa Barbara, Santa Barbara, CA 93106, USA
[4)]Institute for Research and Development in Microtechnologies, 077190 Bucharest, Romania
[5)]Maryland NanoCenter, University of Maryland, College Park, MD 20742, USA

[a)] Electronic mail: brian.hoskins@nist.gov

Metal oxide resistive switches are increasingly important as possible artificial synapses in next generation neuromorphic networks. Nevertheless, there is still no codified set of tools for studying properties of the devices. To this end, we demonstrate electron beam induced current measurements as a powerful method to monitor the development of local resistive switching in TiO$_2$ based devices. By comparing beam-energy dependent electron beam induced currents with Monte Carlo simulations of the energy absorption in different device layers, it is possible to deconstruct the origins of filament image formation and relate this to both morphological changes and the state of the switch. By clarifying the contrast mechanisms in electron beam induced current microscopy it is possible to gain new insights into the scaling of the resistive switching phenomenon and observe the formation of a current leakage region around the switching filament. Additionally, analysis of symmetric device structures reveals propagating polarization domains.

I. INTRODUCTION

Metal oxide resistive switches (also known as ReRAM or memristors) have been of

intense interest for use in next generation memory or as analog weights in neuromorphic

networks[1-3]. Their unique properties, including 2-terminal structure, scalability (more than 10

nm), nonvolatility (more than 10 years at 85 °C), high endurance (more than 10^{12} cycles), and

low energy consumption (less than 10 pJ), are ideal for next generation hardware[4-6]. However,

the complex nature of the switching in these devices, speculated to involve coupling of chemical, electrical, and thermal fields, has stymied a comprehensive understanding of the process[7].

A metal oxide resistive switch consists of two metallic layers separated by a substoichiometric oxide and acts as a programmable resistor. While the switching process is not fully understood, it is generally believed to involve the motion of oxygen vacancies and metal cations in the oxide under electrical fields and thermal gradients[8-10]. This ion motion leads to a local, nanometer-scale variation in the vacancy concentration and a corresponding variation in the thickness of the oxide's depletion region. The vacancy concentration often appears to grow like a metallic, nanoscale filament, and as the depletion region thickness declines, the conductance passes from being controlled by thermionic emission, to being controlled by thermionic field emission, and ultimately to being controlled by field emission.

Several studies have been conducted probing the underlying physics of the switching and exploring the origin and dynamics of filament formation in resistive switches. However, work so far has not yielded a comprehensive picture. Transmission electron microscopy studies suggest that the underlying structural changes during switching can be small, particularly under conditions where the switching is controlled by current compliance[11]. Investigations using scanning transmission x-ray microscopy have probed the chemical changes in devices through the forming process, but have not managed to view single cycle changes or correlate observed large area chemical changes with local changes in the conductivity[12,13]. The chemical variations between conductive and insulating configurations are highly localized and are therefore hard to quantify with available spectroscopic tools, particularly in the presence of a large deformation region[14]. Measurements with scalpel scanning probe microscopy (SPM) have provided precise

measurements of filament behavior. However, the destructive nature of this technique makes it difficult to explore the full parameter space, since it only analyzes a single switching event[15].

In the present work, we employ high resolution scanning electron microscopy (SEM)-based electron beam induced current microscopy (EBIC) to systematically explore switching in TiO_2 devices such as in Figures 1.a and 1.b. We present detailed imaging of filament formation as a function of resistive state (see Figures 1.c and 1.d), and also explore the physical mechanisms of current generation. EBIC has been used previously to characterize resistive switching devices, but relatively low resolution (approximately 1 μm) and the absence of a fundamental understanding of the mechanisms of image formation – due to a lack of stateful and energy dependent data – has so far made it impossible to draw conclusions as to the origin of the generated current and the nature of the filament and its surrounding deformation region[16,17]. By exploring variations in the generated signal in different device geometries (Figure 1.e) as a function of beam energy and resistive state, we show it is possible to probe the underlying physics of the resistive switching devices, clarify the image formation mechanisms, and develop a reliable means of observing filament formation and distinguishing it from non-filament areas. This approach to stateful characterization is robust to measurement artifacts by being selective to the reversible changes in the device and only those regions electrically connected to the circuitry. To provide the most possible information, three different kinds of metal oxide resistive switches (Figure 1.e) were constructed: asymmetric structures were made in a standard form, $Pt\backslash TiO_x\backslash TiN\backslash Pt$, and an inverted form, $Pt\backslash Ti\backslash TiO_x\backslash Pt$, and a symmetric form, $Pt\backslash TiO_x\backslash Pt$, was also made.

In EBIC, few-electron-volt secondary electrons and electron-hole pairs created by a primary beam at 250 eV to 25 keV (Figure 1.a) interact strongly with the built-in device fields.

Current is collected via auxiliary electrodes connected to different parts of the device (Figure 1.b), resulting in a local measurement of the electronic structure stimulated by the incident electron beam[18].

The large number of interfaces in a metal-insulator-metal (MIM) structure such as a metal oxide resistive switch leads to competing currents that sum to the measured EBIC current (I_{EBIC}). We can write:

$$I_{EBIC} = I_{EBAC} + I_{SEE} + I_{e\leftrightarrow h} + I_{ISEE}^{T\rightarrow B} + I_{ISEE}^{B\rightarrow T}, \tag{Eq. 1}$$

where I_{EBAC} is the current absorbed from the incident electron beam (incident current less any backscattered or transmitted current), I_{SEE} is the secondary electron emission current, $I_{e\leftrightarrow h}$ is the electron-hole-pair separation current, $I_{ISEE}^{T\rightarrow B}$ is the internal secondary electron current from the top electrode to the bottom electrode, and $I_{ISEE}^{B\rightarrow T}$ is the internal secondary electron current from the bottom electrode to the top electrode. Figure 2 shows approximate locations of the sources of these currents and their polarities. I_{EBAC} and I_{SEE} are universal to all materials, since they represent the injected current and emitted electrons to vacuum. $I_{e\leftrightarrow h}$, produced when e-beam-induced electron-hole pairs are created at junctions between materials and separated by built-in fields, is often the largest and most commonly measured EBIC partition[19-21]. $I_{ISEE}^{T\rightarrow B}$ and $I_{ISEE}^{B\rightarrow T}$ are unique to MIM structures and result from thermionic emission, diffusion, or tunneling of hot electrons from one electrode to the other[22-24]. In a conventional MIM diode, the internal secondary electron currents are usually negligible, but become measurable at large applied biases (V_b) due to a lowering of the effective barrier height.

Each current can be a probe of the device behavior, e.g. indicating morphological changes such as crystallization or coarsening. Since barrier lowering and raising is

resistive switching, measurable quantities of $I_{ISEE}^{T \to B}$ and $I_{ISEE}^{B \to T}$ are observable in the absence of an applied bias when the device is switched to the on-state, increasing the probability of hot electron transmission.

It can be difficult to deconvolve the sources of current in the device. However, a general principle of EBIC is that the observed current and electron yield, Y_{EBIC} (or nanoampere of signal per nanoampere of injected current), is proportional to the energy deposited into the specific layer sourcing the current. Since beam penetration and absorption primarily depend on the incident beam energy, the ratios of different current contributions will likewise depend on the incident beam energy[25]. Variations in these ratios are predicted by simulating the energy absorbed using Monte Carlo electron simulators[26-28]. Figure 2 shows a 2-dimensional projection, and Figure 3.a shows a 1-d depth profile, for these processes in a Pt\TiO$_x$\TiN\Pt structure for different energies. Integrating all of the energy between two depths as a function of beam voltage makes it possible to define energy absorption functions for different regions of the device $f_{absorbed}^{Top\,Electrode}$ (Figure 3.b), $f_{absorbed}^{TiO_2}$ (Figure 3.c), and $f_{absorbed}^{Bottom\,Electrode}$ (Figure 3.d), which simulate the amount of energy absorbed in each device layer per electron. These can be used to predict currents sourced from those layers such as $I_{ISEE}^{T \to B}$, $I_{e \leftrightarrow h}$, and $I_{ISEE}^{B \to T}$ or their normalized yields respectively.

Here we will show that it is possible to faithfully reproduce the EBIC energy dependence of a ReRAM device as a function of state, using only the independently measured fabrication parameters of the device, the independently modeled e-beam-matter interaction, and physical intuition of a device's internal electrical fields and resistance.

Collectively these can be used to deconstruct complicated effects such as hot electron transmission, material recrystallization, parasitic leakage, and built-in field inversion.

II.   RESULTS

Virgin device measurements

In measurements of virgin asymmetric devices, the EBIC signal arises from an electron flow from low work function (TiN) to high work function contacts (Pt). Consequently, standard device structures exhibited negative absolute current, and inverted structures exhibited positive absolute current (Figure 4.a). Symmetric structures were observed to have a more complex behavior, occasionally exhibiting one polarity or the other as well as significant relaxation and charging of the pad (See Supplementary Note 4).

The energy dependence of the EBIC signal for the different device structures followed the Monte Carlo simulations of energy absorbed in the TiO_x, achieving maximum amplitude at 3.5 keV and 2 keV for the standard and inverted structures, respectively (Figure 4.b). For the standard structure (a top TiN layer) the signal polarity switches from positive to negative at energies above 1 keV, as the secondary electron emission into the vacuum (at low energy) is overcome by the background hole-pair signal (note that the secondary electron emission signal is not included in the Monte Carlo model)[29]. EBIC micrographs of the devices showed strong contrast from the surrounding isolation and electrodes (Figures 4.c-d).

The internal quantum efficiency of the EBIC process can be estimated by combining the simulations with the Alig and Bloom relation[30,31]:

$$E_i \approx 3E_g + 1 \ eV, \tag{Eq. 2}$$

where E_i (the effective pair creation energy) is substituted for E_g (the band gap) in calculations for collection efficiency, η, such that:

$$\eta \approx \frac{E_i}{E_{absorbed}}\frac{I_{EBIC}}{I_{beam}} = \frac{E_i}{E_{absorbed}}Y_{EBIC}, \tag{Eq.3}$$

where I_{EBIC} and I_{beam} are the measured EBIC and incident beam currents respectively and Y_{EBIC} is the resulting yield from their ratio[32]. For the standard structure at 5 keV, the simulation predicts that approximately 50 electron-hole pairs per incident electron should be generated, as opposed to an approximately measured 4 electron-hole pairs, suggesting a collection efficiency of 8 %.

Switched device, asymmetric structure

Switched-on devices exhibited morphological changes including electrode changes, both minor and severe, visible by the secondary electron detector, as well as morphological changes in TiO$_2$ visible in the EBIC signal. Minor changes in the electrode include grain coarsening which was easily visible as increased secondary electron emission (or image brightening) relative to the unaffected areas[33-36]. More severe changes include tearing of the electrode. For measurements potentially sensitive to changes in the electrode, devices with torn electrodes were not used.

In what follows, the signal discussed refers to the change in EBIC current relative to the current measured in virgin structures (the background current). Energy dependent beam measurements of the device in both the off and the on state (Figure 5) show a strong dependence on the device resistivity in both the polarity and magnitude of the signals. In the off state, the formed region shows a region of enhanced dark contrast which could be as small as 100 nm in diameter to as large as 300 nm. Its signal

maximum, between 2.5 and 5 keV, suggests it is due to an enhanced electron-hole pair current, $I_{e\leftrightarrow h}$, arising from crystallization of the oxide, which is known to be a consequence of forming resistive switches[11,17,36].

Within this broader darker region, which we will call the crystallized region, a new, positive signal appears at low beam energies in the on-state. This positive signal correlates with the state of the device, and vanishes when the device is programmed into the off state – indicating the signal is associated with the filament. Measurements as a function of energy showed that the signal achieves a maximum at 1.5 keV, a value consistent with top electrode absorption (Figure 3.b). The polarity and beam energy of the signal maximum suggest that the EBIC signal is due to internal secondary electron emission (ISEE). This is further supported by determining whether the polarity of the filament signal remains unchanged in the inverted devices. Since beam-electrode collisions generate hot electrons, the signal current polarity should be independent of the filament orientation, and, indeed, inverting the device did not cause a reversal in the polarity of the signal (See Supplementary Note 6).

A clearer picture of the different current contributions as a function of state can be obtained by doing azimuthal integration to average around the filament location and then plotting the radial current distribution. Figure 6.a shows the off state distribution with a bottom plateau and a broad, ill-defined edge region where $I_{e\leftrightarrow h}$ declines monotonically to the background, possibly corresponding to a transition between polycrystalline and the surrounding amorphous regions. Figures 6.b and 6.c show the change in the on-state profiles with increasing beam energy. The plot of the internal secondary electron emission from the top electrode to the bottom electrode $I_{ISEE}^{T\rightarrow B}$ shows significant

broadening from the diffusion hot of electrons across the top electrode to the filament. At 5 keV it is significantly mixed with both the internal secondary electron emission from the bottom electrode to the top electrode, $I_{ISEE}^{B \to T}$, and the electron-hole pair separation current, $I_{e \leftrightarrow h}$, causing oscillations to begin emerging. At the highest beam energies, $I_{ISEE}^{B \to T}$ and $I_{e \leftrightarrow h}$ exhibit a substantially higher fraction of the total overall signal and the narrower diffusion widths and smaller magnitudes of $I_{ISEE}^{B \to T}$ and $I_{e \leftrightarrow h}$ create an oscillatory cross-section of the EBIC profile.

The energy dependencies of the signals can be more carefully considered by using the Monte Carlo modeled energy absorption functions $(f_{absorbed}^{Top\ Electrode}, f_{absorbed}^{Bottom\ Electrode}, f_{absorbed}^{TiO_2})$ to model the electron yields $(Y_{ISEE,On(Off)}^{T \to B}, Y_{ISEE,On(Off)}^{B \to T}, Y_{e \leftrightarrow h})$ as a function of energy. Each of the absorption functions $f_{absorbed}$ describes the incident energy dependence of all of the energy absorbed in each layer of the device, as well as the expected sign of the resultant EBIC current. Assuming proportionality of the yields to the absorption functions, we write:

$$Y_{ISEE,On(Off)}^{T \to B} = a_{On(Off)} f_{absorbed}^{Top\ Electrode} \qquad \text{Eq. (4)}$$

$$Y_{ISEE,On(Off)}^{B \to T} = a_{On(Off)} \delta f_{absorbed}^{Bottom\ Electrode} \qquad \text{Eq. (5)}$$

$$Y_{e \leftrightarrow h} = c f_{absorbed}^{TiO_2} \qquad \text{Eq. (6)}$$

The constants of proportionality for the ISEE signals $a_{On(Off)}$ have a different value depending on whether the device is in the on or off state. The factor δ is a constant representing the relative yields between $Y_{ISEE}^{T \to B}$ and $Y_{ISEE}^{B \to T}$, and c is a constant describing the electron-hole pair background signal for $Y_{e \leftrightarrow h}$. Both c and δ are taken to be state-

independent. The total EBIC yield $Y_{EBIC}^{On(Off)} = Y_{ISEE,On(Off)}^{T \to B} + Y_{ISEE,On(Off)}^{B \to T} + Y_{e \leftrightarrow h}$ can

then be written for the on and off states as:

$$Y_{EBIC}^{On} = a_{On}(f_{absorbed}^{Top\ Electrode} + \delta f_{absorbed}^{Bottom\ Electrode}) + c f_{absorbed}^{TiO_2} \qquad (Eq.7)$$

$$Y_{EBIC}^{Off} = a_{Off}(f_{absorbed}^{Top\ Electrode} + \delta f_{absorbed}^{Bottom\ Electrode}) + c f_{absorbed}^{TiO_2} \qquad (Eq.8)$$

We then allow the four coefficients $a_{On}, a_{Off}, \delta,$ and c to be free parameters in a

simultaneous least-squares fit of both Eq. 7 and 8 to the measured electron yields for the

on and the off state. The result of the fit is shown in Figure 7.

It's apparent from Figure 7 that a simple linear combination model with only four

free parameters can reproduce the most important features of the on-state and off-state

EBIC curves, including the locations of the maximum, minimum, and the decay at high

incident beam energy, with only the coefficient of the ISEE signal changing between the

states. This is done fairly accurately using only the independently measured film

thicknesses from the fabrication as input to the Monte Carlo model, without resorting to

adjustments for tilt or density. This simplistic model does surprisingly well, considering

the underlying complexity of the processes involved. A more detailed model would

likely have to include the details of hot electron transport in diodes in addition to the

energy absorption[22,23].

Scaling of the internal secondary electron emission signal

Tracking the ISEE signal, and by proxy the coefficient a, across a region provides

both a qualitative (See Supplementary Movie 1) and a quantitative measure of the barrier

to hot electron conductance and its scaling with device resistance. This can be done by

continuously tuning the device resistance and measuring the change in total signal at a

single beam energy. Summing up the total differential current with respect to the off-

state through a turn-on and turn-off event, it is apparent that the ISEE signal follows a power law with exponent less than 1 as a function of conductance as the device is programmed into the off-state (Figure 8.a), and scales nearly linearly with conductance as the device is programmed into the on-state (Figure 8.b). The different scaling relationships between the turn-on and turn-off branches suggest contrasting mechanisms for the filament formation and dissolution respectively.

One interpretation suggests that the on-branch switching is area dependent, driven by nucleation, saturation, and expansion of the filament, producing a signal proportional to the area (A), whereas the turn-off process is barrier dependent (through φ_{eff}, an effective barrier to conductance), and therefore determined entirely by a local state variable (such as the oxygen vacancy concentration). Such a difference has been proposed in some thermophoresis-based models of resistive switching[37,38]. In drift-diffusion models it is potentially possible to explain based on the differing dopant profiles produced by drift/diffusion acting in concert or in opposition to one another, as well as by including 2-dimensional effects [37,39].

In filaments models, competing modes of conduction often include Poole-Frenkel emission, space charge limited conduction, and interfacial resistance depending on the resistive state[40,41]. These models capture the most attractive feature of resistive switches, i.e., the ability to continuously tune their resistance by varying some effective barrier height, φ_{eff}, between maximal (φ_{off}) and minimal (φ_{on}) values. In the case of TiO_2, the device resistance is often modeled as being controlled by an interfacial Schottky junction with a variable Arrhenius factor controlled by an exponent, $\frac{\varphi_{\mathrm{eff}}}{k_{\mathrm{B}}T_{\mathrm{o}}}$,[42-45]. This approach is also sometimes used for other systems, especially $SrTiO_3$[46-48]. While it can be fairly

11

accurate for the off-state, its accuracy will decline in the limit of high conductivity as

field emission dominates the transport across the interface and the conductance becomes

limited by the quantum or Sharvin point contact resistance[49]. In this case, the temperature

dependence could be expected to change from insulating to metallic[50]. However, it will

be used here as a first approximation of the relationship between the conductance and the

ISEE signal.

The scaling relationships during the turn-on and turn-off branches can be analyzed

assuming the zero-bias conductance σ follows the behavior of a Schottky junction,

$$\sigma = \frac{dI_{\text{Schottky}}}{dV}\Big|_{V=0} = \alpha A e^{-\frac{\varphi_{\text{eff}}}{k_{\text{B}}T_0}}, \qquad\qquad \text{(Eq. 9)}$$

where α is a prefactor, A is the area of the filament, φ_{eff} is the effective barrier height,

and T_0 is the ambient temperature[51]. The ISEE signal can be assumed to follow

thermionic emission theory, with a characteristic hot electron temperature, T_{e}, such

that[22,23]

$$I_{\text{ISEE}} = \beta A e^{-\frac{\varphi_{\text{eff}}}{k_{\text{B}}T_{\text{e}}}}. \qquad\qquad \text{(Eq. 10)}$$

Assuming the barrier height is constant, as might occur if nucleation and growth

dominates in the turn-on branch, the two values will be proportional to one another.

Consequently the ISEE signal should obey:

$$I_{\text{ISEE turn-on}} \sim \frac{\beta}{\alpha}\sigma, \qquad\qquad \text{(Eq. 11)}$$

This relationship between the I_{ISEE} and σ is unsurprising since it is very similar to the

well studied relationship between the turn-on switching compliance current, device

conductance, and filament area which are also all thought to be proportional[52]. If,

however, the effective barrier height varies due to barrier lowering, then the scaling

between I_{ISEE} and σ can be modeled by:

$$I_{\text{ISEE Turn-off}} = \frac{A\beta}{(A\alpha)^{\frac{T_{\text{o}}}{T_{\text{e}}}}}\sigma^{\frac{T_{\text{o}}}{T_{\text{e}}}}, \qquad\qquad\text{(Eq. 12)}$$

where $\frac{T_{\text{o}}}{T_{\text{e}}}$ is the exponent in a power law scaling between the ISEE signal and the

conductivity. Since the hot electron temperature is greater than ambient, $\frac{T_{\text{o}}}{T_{\text{e}}}$ should be

strictly less than unity. The extracted value of 0.44 is consistent with this, suggesting an

average hot electron temperature of 700 K. While this is a reasonable value for T_{e}, other

models are possible and T_{e} may depend on the model chosen. Understanding the scaling

between fit parameters and values extracted from other methods, such as the temperature

coefficient of resistivity of the device, may help clarify these underlying mechanisms[53].

Imaging the effects of leakage currents around the filament

Comparing an initial state of the device (Figure 9.a-b) after a stress test (Figure

9.c) to a subsequent device state (Figure 9.d), can provide insights on the distribution of

current and power during switching. In the area surrounding the filament, we observe a

surrounding dark contrast, most likely crystallized region, which appears to act as a non-

programmable leakage path through which excess current can flow (Figure 9.e). Forward

biasing the junction during turn-off leads to significant power dissipation, with a

maximum occurring at -1.7 V and a leakage current of 2 mA (Figure 9c). Device cycling

can lead to electrode coarsening in the crystallized region, and this was observed after a

10-cycle test (Figure 9.c). The SEM images before (Figure 9.a) and after (Figure 9.d)

reveal increased secondary electron emission, caused by grain coarsening, in the regions

corresponding to the leakage[33-36,54]. It's important to note that power must be dissipating

in this region, since electrical connectivity is a precondition for imaging in EBIC, and so the enhanced secondary electron emission is not a sign of the electrode delaminating, which would cause the signal to vanish or share similar magnitude to its immediate neighbors, from where carriers can diffuse. This correlation of power dissipation with the crystallization region, as opposed to being centered on the filament, suggests that managing damage induced by the filament formation is more important than controlling changes to the filament itself. Reducing the device size below the breadth of the crystallization region is the simplest possible means of reducing the leakage and excess power dissipation.

With the current density in this region running at approximately $7.8 \cdot 10^{10}$ A m^{-2} during the turn off process, a reduction to a 10 nm $\times$ 10 nm structure would reduce the leakage to 6 µA. Adding interfacial layers or otherwise engineering the device could also yield benefits by changing the specific contact resistance. While current limiters such as integrated transistors or ultra-fast pulses are commonly used to manage current overshoot and device damage, passive means to mitigate the effects of overheating the surrounding device region may be critical for some applications, like passive crossbar arrays[1,55,56].

Switched device symmetric structure

The questions of scaling and polarization take on new meaning in a symmetric device with dual Pt electrodes. In the asymmetric structures, overdriving the devices leads to electrode degradation and migration of the switching spot to a new location, however the underlying switching characteristics do not change. Degradation is also present in symmetric structures, but coexists with domains of programmable polarization. This was observed by increasing the voltage stress and cycling the bias between negative

and positive polarities, which led to increasing amplitude changes in the orientation of the built-in electric fields as measured by EBIC (Figures 10.a-d and 10.j).

A stepwise motion through the switching reversal (Figures 10.e-i) reveals a propagating domain wall. A measure of the total integrated signal through this transition shows a maximum in the conductivity as the signal sum passes through zero, suggesting highest conductivity when the two polarizations are in balance, with a large domain wall between them (Figure 10.k). The theory of complementary resistive switching suggests that the conductivity will be highest at the interface between these two regions, and so the power dissipation and switching will be preferentially located here (Figures 10.h and 10.l) inducing its propagation[42,46,57]. We observed that some boundaries were less mobile than the primary one, which may be due to local variations in the grain orientation, crystallinity, or in the composition induced by the high stress.

The differences between the symmetric and asymmetric structures can be attributed to the competing scaling relationships that characterize them. As an asymmetric device is further polarized, its conductivity will only increase until some physical limit, like the temperature of melting, is reached. This is also true in the case of symmetric structures, but a sufficiently polarized device will ultimately decrease in conductivity due to field reversal. The reduction in dissipated power provides an opportunity for adjacent regions to also switch and likewise undergo inversion without the total power dissipation becoming large. This suggests that changes to the device structure, such as the asymmetry, specific resistance, or the heat dissipation change the scaling of the switching.

III. Discussion

Understanding the physics of EBIC imaging in resistive switching devices has broader implications for the metrology of resistive switching. The direct observation of hot electron currents, for example, opens the door to other hot electron techniques such as ballistic electron emission microscopy (BEEM) and internal photoemission (IPE)[58-60]. IPE, being the optical analog to EBIC, sacrifices spatial resolution for precise spectroscopic information. While IPE has long been used to study MIM diodes and other electronic devices[59,61], its use has not been demonstrated on filaments, probably due to the small active area. An IPE system, most likely combined with high brightness sources, focusing optics and phase sensitive detection, could make it possible to deconstruct the underlying electronic structure of the filament-electrode interface as a function of state.

Though EBIC is clearly applicable for conventional device geometries, our results also show its applicability for other geometries, like lateral devices. If the devices studied here were rotated on their side, with EBIC it would be possible to probe the device depletion region at its interface, as in conventional EBIC, and also determine the onset of filament formation by observing the emergence of ISEE at the electrodes. With a lateral device, it would be easier to see structural changes (such as with electron back scattering diffraction or X-ray absorption) as the device switches, but this could also lead to false positives as regions unrelated to the switching are changed by Joule heating. This problem is particularly acute at large biases where leakage currents could dominate the electrical properties, as seen in Figure 9. EBIC then can be an effective, rapid means of disentangling resistive switching from artifacts.

We demonstrate energy dependent and stateful EBIC measurements on conventional resistive switching devices. Comparing these measurements to Monte Carlo

simulations reveals two competing forms of contrast that have not previously been distinguished: classic electron-hole pair separation, and internal secondary electron emission (ISEE). Differentiating between these two forms of current generation makes it possible to distinguish the filament from its surrounding recrystallized region. Stateful measurements of the ISEE current show different scaling relationships for the turn-on and turn-off branches, which suggests the existence of different, hysteretic mechanisms for filament formation and dissolution. Symmetric device structures show propagating fronts of different polarizations, depending on the direction of the applied bias prior to the image acquisition. This large area switching suggests that the details of device manufacture and geometry can have a significant effect on the underlying scaling of the resistive switching. These effects are difficult to observe spectroscopically, but become clear with EBIC.

Methods
Electrical Setup and Current Measurements

Samples were mounted in a conventional Schottky-emission SEM with electrical feedthroughs connected to the device and a stage-mounted Faraday cup for calibrating the injected current. Measurements were done in cycles of grounding the device, programming the device with a source-measure unit, grounding the device, connecting the current amplifier, and then imaging the device. The effect of changing the device conductance (as measured at 0.1 V) was probed by observing the EBIC signal at individual locations on the device as well as by summing the total signal within an image after subtracting the background due to the surrounding pristine area. Comparing the change in total integrated EBIC signal with respect to the off-state compactly quantifies changes in the state of the device. The image formation mechanisms were probed by imaging the same locations repeatedly with beam energies from 250 eV to 25 keV and then measuring the beam current for each. Plotted ratios of injected beam current to EBIC current (the electron yield, Y_{EBIC}) were compared to layer-by-layer energy absorption plots predicted from Monte Carlo simulations of low energy electrons in the different device structures to determine the origins of different currents[28,62].

Image Processing

Extracted images are sensitive to effects such as beam-device interactions, 60 Hz noise, device noise, and current-amplifier drift. To minimize these effects, the images were processed using Fourier masking and mean-line leveling to minimize noise and data

acquisition artifacts. The images were aligned by doing least-squares minimization of the SEM images and their image off-sets. More information is available in Supplementary Note 2.

Monte Carlo Simulations

These simulations took as inputs conventionally available values of the density for the materials used as well as independently calibrated film thicknesses from the device fabrication (See Supplementary Note 3). Ten thousand electron trajectories were averaged at a given energy (from 250 eV to 25 keV) to produce a 3-dimensional model of the energy absorbed in the device. 2-D and 1-D plots were generated by numerically integrating all the energy in an individual voxel to produce plots with units of keV nm^{-2} and keV nm^{-1} respectively.

Device Fabrication

The devices were fabricated with a combination of sputtering and e-beam evaporation. Pt bottom electrodes were sputtered and patterned by Ar ion milling. Subsequently TiO_x was reactively sputtered with an in-situ top electrode[63]. The top electrode was ion milled in a mixture of Ar and O_2. SiO_2 isolation was patterned by liftoff, with undercut providing a gentle slope. The top electrode contact and subsequent large contacts were deposited by e-beam evaporation of Ti/Au. More details are available in Supplementary Note 1.

Forming Process

In addition to conventional voltage-induced forming, we also used beam-induced defect formation to improve the reliability of the forming process[64,65]. We found that the dielectric breakdown needed to create switching could be initiated by the combined application of voltage (either current sweeps or voltage pulses) and a large e-beam current at 5 keV. This electron beam assisted forming process made it possible to deterministically locate the breakdown region and consequently the filament (See Supplementary Note 5). A 5 kΩ series resistor was used to limit the current.

Data Availability

All data is available on reasonable request of the corresponding author. A summary of many important IV curves and images is available in Supplementary Note 7.

References

1.   Adam, G.C.*, et al.* 3-D Memristor Crossbars for Analog and Neuromorphic Computing Applications. *IEEE Trans. Electron Devices* **64**, 312-318 (2017).

2.   Adam, G.C., Hoskins, B.D., Prezioso, M. & Strukov, D.B. Optimized stateful material implication logic for three-dimensional data manipulation. *Nano Research* **9**, 3914-3923 (2016).

3.   Prezioso, M.*, et al.* Training and operation of an integrated neuromorphic network based on metal-oxide memristors. *Nature* **521**, 61-64 (2015).

4.   Yang, J.J., Strukov, D.B. & Stewart, D.R. Memristive devices for computing. *Nature Nanotechnol.* **8**, 13-24 (2013).

5.   Yang, J.J.*, et al.* High switching endurance in TaO_x memristive devices. *Appl. Phys. Lett.* **97**, 232102 (2010).

6.   Govoreanu, B.*, et al.* 10x10nm Hf/HfO_x crossbar resistive RAM with excellent performance, reliability and low-energy operation. in *IEEE International Electron Devices Meeting (IEDM)* 31.36.31-31.36.34 (2011).

7.   Kim, S., Choi, S. & Lu, W. Comprehensive Physical Model of Dynamic Resistive Switching in an Oxide Memristor. *ACS Nano* **8**, 2369-2376 (2014).

8.   Strukov, D.B., Borghetti, J.L. & Williams, R.S. Coupled Ionic and Electronic Transport Model of Thin-Film Semiconductor Memristive Behavior. *Small* **5**, 1058-1063 (2009).

9.   Menzel, S.*, et al.* Origin of the Ultra-nonlinear Switching Kinetics in Oxide-Based Resistive Switches. *Adv. Funct. Mater.* **21**, 4487-4492 (2011).

10.   Strukov, D.B., Alibart, F. & Stanley Williams, R. Thermophoresis/diffusion as a plausible mechanism for unipolar resistive switching in metal–oxide–metal memristors. *Appl. Phys. A* **107**, 509-518 (2012).

11.   Kwon, J.*, et al.* Transient Thermometry and High-Resolution Transmission Electron Microscopy Analysis of Filamentary Resistive Switches. *ACS Appl. Mater. Interfaces* **8**, 20176-20184 (2016).

12.   Strachan, J.P.*, et al.* Spectromicroscopy of tantalum oxide memristors. *Appl. Phys. Lett.* **98**, 242114 (2011).

13.   Kumar, S.*, et al.* Direct Observation of Localized Radial Oxygen Migration in Functioning Tantalum Oxide Memristors. *Adv. Mater.* **28**, 2772-2776 (2016).

14.   Yang, J.J.*, et al.* The mechanism of electroforming of metal oxide memristive switches. *Nanot* **20**, 215201 (2009).

15.   Celano, U.*, et al.* Imaging the Three-Dimensional Conductive Channel in Filamentary-Based Oxide Resistive Switching Memory. *Nano Lett.* **15**, 7970-7975 (2015).

16.   Rossel, C., Meijer, G.I., Brémaud, D. & Widmer, D. Electrical current distribution across a metal–insulator–metal structure during bistable switching. *J. Appl. Phys.* **90**, 2892 (2001).

17.   Yi Meng, L.*, et al.* Elimination of high transient currents and electrode damage during electroformation of TiO_2 -based resistive switching devices. *J. Phys. D: Appl. Phys.* **45**, 395101 (2012).

18.   Ioannou, D.E. & Dimitriadis, C.A. A SEM-EBIC minority-carrier diffusion-length measurement technique. *IEEE Trans. Electron Devices* **29**, 445-450 (1982).

19.   Yoon, H.P.*, et al.* Local electrical characterization of cadmium telluride solar cells using low-energy electron beam. *Sol. Energy Mater. Sol. Cells* **117**, 499-504 (2013).

20.   Haney, P.M., Yoon, H.P., Koirala, P., Collins, R.W. & Zhitenev, N.B. Electron beam induced current in the high injection regime. *Nanot* **26**, 295401 (2015).

21.   Kittler, M. & Seifert, W. On the origin of EBIC defect contrast in silicon. A reflection on injection and temperature dependent investigations. *Phy. Status Solidi A* **138**, 687-693 (1993).

22.   Hanke, S.*, et al.* Computer simulation of internal electron emission in ion-bombarded metals. *Nucl. Instrum. Methods Phys. Res., Sect. B* **303**, 55-58 (2013).

23.   Hanke, S., Duvenbeck, A., Heuser, C., Weidtmann, B. & Wucher, A. A hybrid model describing ion induced kinetic electron emission. *Nucl. Instrum. Methods Phys. Res., Sect. B* **352**, 18-21 (2015).

24.   Lin, P. & Leamy, H. Tunneling current microscopy. *Appl. Phys. Lett.* **42**, 717-719 (1983).

25.   Goldstein, J.*, et al. Scanning Electron Microscopy and X-Ray Microanalysis: A Text for Biologists, Materials Scientists, and Geologists*, (Springer US, 2013).
26.   Hovington, P., Drouin, D., Gauvin, R., Joy, D.C. & Evans, N. CASINO: A new Monte Carlo code in C language for electron beam interactions—part III: Stopping power at low energies. *Scanning* **19**, 29-35 (1997).
27.   Drouin, D., Hovington, P. & Gauvin, R. CASINO: A new monte carlo code in C language for electron beam interactions—part II: Tabulated values of the mott cross section. *Scanning* **19**, 20-28 (1997).
28.   Drouin, D.*, et al.* CASINO V2.42—A Fast and Easy-to-use Modeling Tool for Scanning Electron Microscopy and Microanalysis Users. *Scanning* **29**, 92-101 (2007).
29.   Dionne, G.F. Origin of secondary-electron-emission yield-curve parameters. *J. Appl. Phys.* **46**, 3347 (1975).
30.   Alig, R. & Bloom, S. Electron-hole-pair creation energies in semiconductors. *Phys. Rev. Lett.* **35**, 1522 (1975).
31.   Glavatskikh, I.A., Kortov, V.S. & Fitting, H.J. Self-consistent electrical charging of insulating layers and metal-insulator-semiconductor structures. *J. Appl. Phys.* **89**, 440 (2001).
32.   Haney, P.M., Yoon, H.P., Gaury, B. & Zhitenev, N.B. Depletion region surface effects in electron beam induced current measurements. *J. Appl. Phys.* **120**, 095702 (2016).
33.   Kawata, J. & Ohya, K. Surface Roughness Effect on Secondary Electron Emission from Beryllium under Electron Bombardment. *J. Phys. Soc. Jpn.* **63**, 795-806 (1994).
34.   Yong, Y.C., Thong, J.T.L. & Phang, J.C.H. Determination of secondary electron yield from insulators due to a low-kV electron beam. *J. Appl. Phys.* **84**, 4543-4548 (1998).
35.   Kawata, J., Ohya, K. & Nishimura, K. Simulation of secondary electron emission from rough surfaces. *J. Nucl. Mater.* **220**, 997-1000 (1995).
36.   Lu, Y.M.*, et al.* Impact of Joule heating on the microstructure of nanoscale TiO2 resistive switching devices. *J. Appl. Phys.* **113**, 163703 (2013).
37.   Mickel, P.R.*, et al.* A physical model of switching dynamics in tantalum oxide memristive devices. *Appl. Phys. Lett.* **102**, 223502 (2013).
38.   Mickel, P.R., Lohn, A.J., Mamaluy, D. & Marinella, M.J. Power signatures and vacancy profile control in nanoscale memristive filaments. *Appl. Phys. Lett.* **107**, 033507 (2015).
39.   Mickel, P.R., Lohn, A.J., James, C.D. & Marinella, M.J. Isothermal Switching and Detailed Filament Evolution in Memristive Systems. *Adv. Mater.* **26**, 4486-4490 (2014).
40.   Yang, Y., Choi, S. & Lu, W. Oxide Heterostructure Resistive Memory. *Nano Lett.* **13**, 2908-2915 (2013).
41.   Yu, S., Guan, X. & Wong, H.S.P. Conduction mechanism of TiN∕HfOx∕Pt resistive switching memory: A trap-assisted-tunneling model. *Appl. Phys. Lett.* **99**, 063507 (2011).
42.   Yang, J.J., Borghetti, J., Murphy, D., Stewart, D.R. & Williams, R.S. A family of electronically reconfigurable nanodevices. *Adv. Mater.* **21**, 3754-3758 (2009).

43.   Yang, J.J.*, et al.* Metal/TiO2 interfaces for memristive switches. *Appl. Phys. A* **102**, 785-789 (2011).

44.   Yang, J.J.*, et al.* Engineering nonlinearity into memristors for passive crossbar applications. *Appl. Phys. Lett.* **100**, 113501 (2012).

45.   Park, J.*, et al.* Multibit Operation of TiO_2 -Based ReRAM by Schottky Barrier Height Engineering. *IEDL* **32**, 476-478 (2011).

46.   Marchewka, A., Waser, R. & Menzel, S. Physical simulation of dynamic resistive switching in metal oxides using a Schottky contact barrier model. in *2015 International Conference on Simulation of Semiconductor Processes and Devices (SISPAD)* 297-300 (IEEE, 2015).

47.   Baeumer, C., *et al.* Quantifying redox-induced Schottky barrier variations in memristive devices via in operando spectromicroscopy with graphene electrodes. *Nat. Comm.* **7**, 12398 (2016).

48.   Hur, J.H., Lee, M.-J., Lee, C.B., Kim, Y.-B. & Kim, C.-J. Modeling for bipolar resistive memory switching in transition-metal oxides. *Phys. Rev. B* **82**, 155321 (2010).

49.   Blonkowski, S. & Cabout, T. Bipolar resistive switching from liquid helium to room temperature. *J. Phys. D: Appl. Phys.* **48**, 345101 (2015).

50.   Walczyk, C.*, et al.* Impact of Temperature on the Resistive Switching Behavior of Embedded HfO_2-Based RRAM Devices. *IEEE Trans. Electron Devices* **58**, 3124-3131 (2011).

51.   Sze, S.M. & Ng, K.K. *Physics of semiconductor devices*, (John wiley & sons, 2006).

52.   Ielmini, D. Modeling the Universal Set/Reset Characteristics of Bipolar RRAM by Field- and Temperature-Driven Filament Growth. *IEEE Trans. Electron Devices* **58**, 4309-4317 (2011).

53.   Miao, F.*, et al.* Continuous electrical tuning of the chemical composition of TaO x-based memristors. *ACS Nano* **6**, 2312-2318 (2012).

54.   Gao, B.*, et al.* In situ transmission electron microscopy imaging of grain growth in a platinum nanobridge induced by electric current annealing. *Nanot* **22**, 205705 (2011).

55.   Nminibapiel, D.M.*, et al.* Characteristics of Resistive Memory Read Fluctuations in Endurance Cycling. *IEDL* **38**, 326-329 (2017).

56.   Shrestha, P.*, et al.* compliance-free pulse forming of filamentary RRAM. *ECS Transactions* **75**, 81-92 (2016).

57.   Schonhals, A.*, et al.* Critical ReRAM Stack Parameters Controlling Complimentary versus Bipolar Resistive Switching. in *IEEE International Memory Workshop (IMW)* 1-4 (IEEE, 2015).

58.   Ludeke, R. Hot electron transport through metal–oxide–semiconductor structures studied by ballistic electron emission spectroscopy. *J. Vac. Sci. Technol. B* **13**, 1830 (1995).

59.   Burshtein, Z. & Levinson, J. Photo-induced tunnel currents in Al-Al_2O_3-Au structures. *Phys. Rev. B* **12**, 3453 (1975).

60.   Durcan, C.A., Balsano, R. & LaBella, V.P. Time dependent changes in Schottky barrier mapping of the W/Si (001) interface utilizing ballistic electron emission microscopy. *J. Appl. Phys.* **117**, 245306 (2015).

61.   Mooney, J.M. & Silverman, J. The theory of hot-electron photoemission in Schottky-barrier IR detectors. *IEEE Trans. Electron Devices* **32**, 33-39 (1985).

62.   Hovington, P., Drouin, D. & Gauvin, R. CASINO: A new Monte Carlo code in C language for electron beam interaction—Part I: Description of the program. *Scanning* **19**, 1-14 (1997).

63.   Hoskins, B.D. & Strukov, D.B. Maximizing stoichiometry control in reactive sputter deposition of TiO2. *J. Vac. Sci. Technol. A* **35**, 020606 (2017).

64.   Madey, T.E. & Jr., J.T.Y. Electron-Stimulated Desorption as a Tool for Studies of Chemisorption: A Review. *J. Vac. Sci. Technol.* **8**, 525-555 (1971).

65.   Smith, D.J., McCartney, M. & Bursill, L. The electron-beam-induced reduction of transition metal oxide surfaces to metallic lower oxides. *Ultramicroscopy* **23**, 299-303 (1987).

Author Contributions

NZ, AK, DBS, BDH, and JJM conceived the experiment. BDH, GCA, and DBS designed the devices. BDH and GCA fabricated the devices. BDH, ES, AK, NZ and JJM developed experimental procedures and designed electronics. BDH performed the measurements and wrote the manuscript. All contributors discussed the experimental results and edited the manuscript.

Acknowledgements

Competing interests:

The authors declare no competing financial interests.
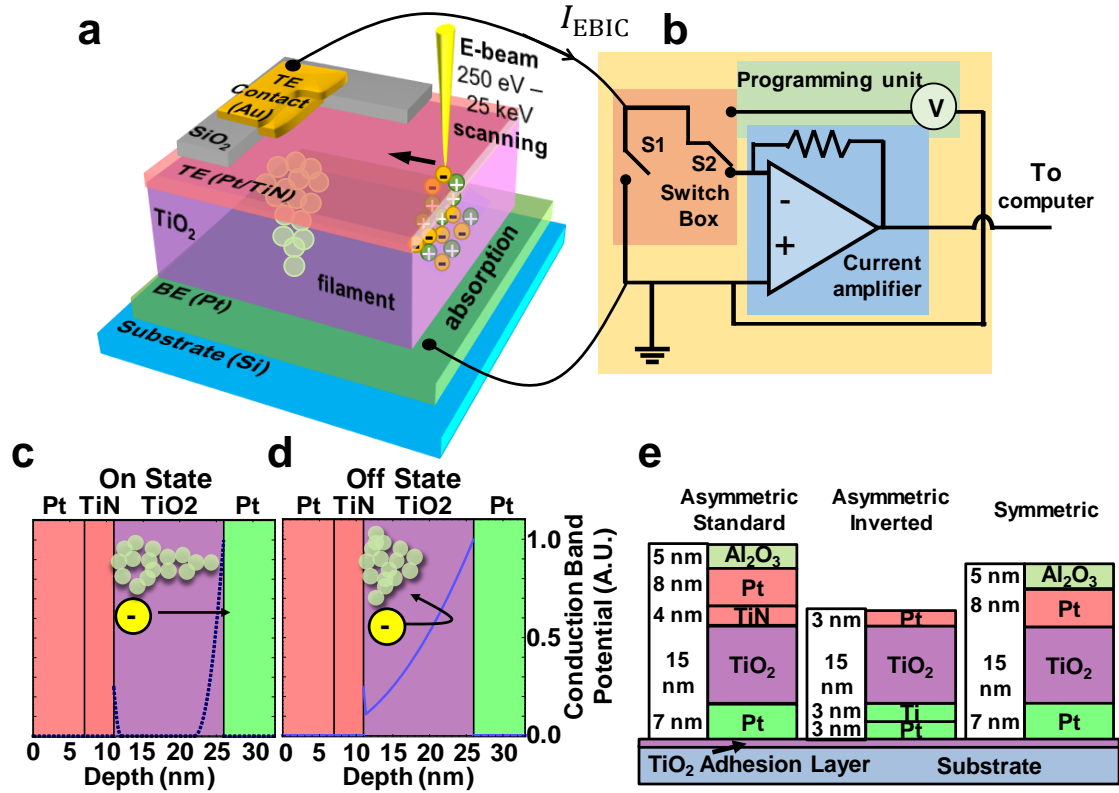
Figure 1. Overview of Experiment. a) 3-D depiction of the experimental EBIC measurement including top electrode (TE, pink), the TE contact (yellow), bottom electrode (BE, green), e-beam with its generated carriers, dielectric layer (TiO2, purple), and the programmable filament. b) Basic electric measurement setup including switch box with grounding switch (S1) and exchange between imaging (with the current amplifier) and programming (S2). c) Simplified schematic depiction of the filament in the on state (spanning the top electrode to the bottom electrode) and d) the off state (leaving an insulating barrier). e) Device stack of the different structures analyzed. The protective aluminum oxide was stripped from the inverted device and the Pt made thinner in an attempt to increase the resolution.
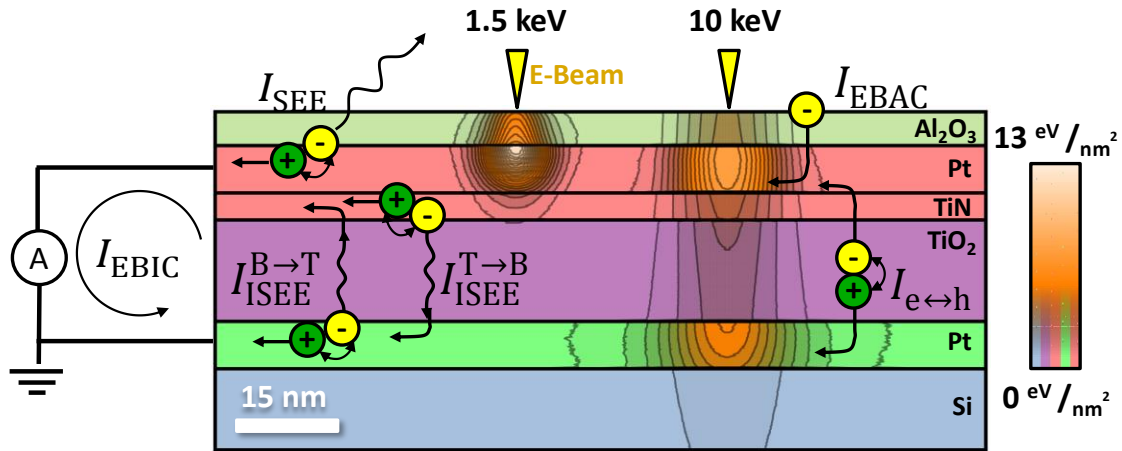

Figure 2. Depiction of device beam interaction. Monte Carlo simulated absorption in a multi-layer ReRAM device at both 1.5 keV incident beam and 10 keV incident beam. Absorption in different layers can result in the different depicted currents including the secondary electron current (I_{SEE}), the electron

beam absorbed current (I_{EBAC}), the electron-hole pair current ($I_{e\leftrightarrow h}$), and the internal secondary electron currents from top-to-bottom ($I_{ISEE}^{T\rightarrow B}$) and bottom-to-top ($I_{ISEE}^{B\rightarrow T}$). These all sum to create the measured electron beam induced current (I_{EBIC}). Energy absorption scale bar indicates high intensity (white), intermediate intensity (orange), and zero intensity (transparent revealing diagram coloring of corresponding device layers).
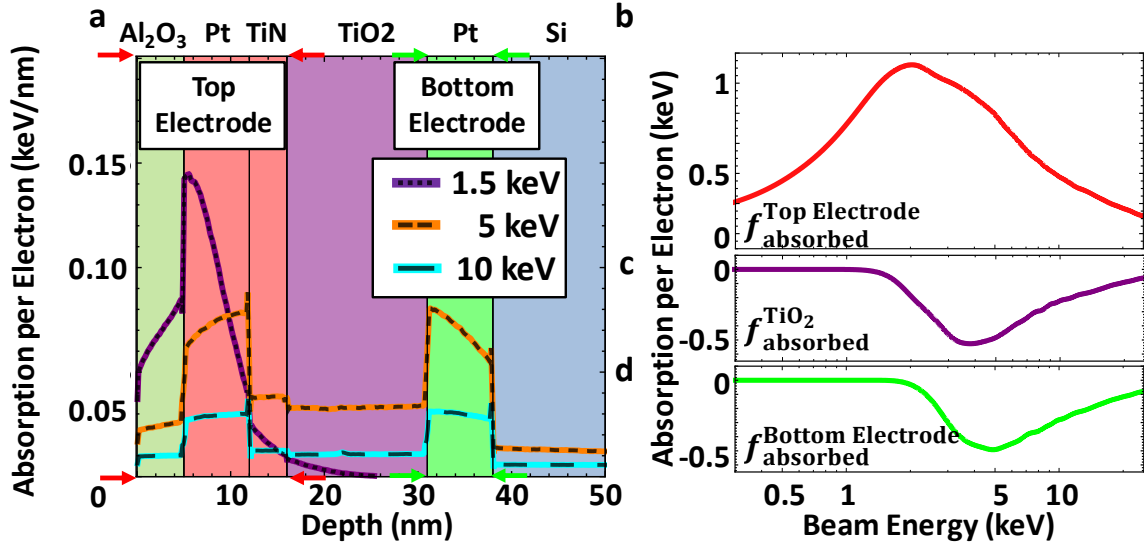

Figure 3. Distribution of energy in device. a) Simulated 1-dimensional absorption profile in an ReRAM stack for different beam energies. Energy absorbed in the TiO_2 layer first rises and then falls with increasing beam energy. Note any energy absorbed in the silicon does not contribute to the measured electron beam induced current. Arrows indicate regions of energy over which Top and Bottom Electrodes are integrated over for the layer-by-layer energy distributions. b-d) Monte Carlo simulations on an asymmetric standard structure of absorption in (b) top layer, (c) TiO_2 layer and (d) bottom layer as a function of beam energy summarizing contributions from all elements of the structure.
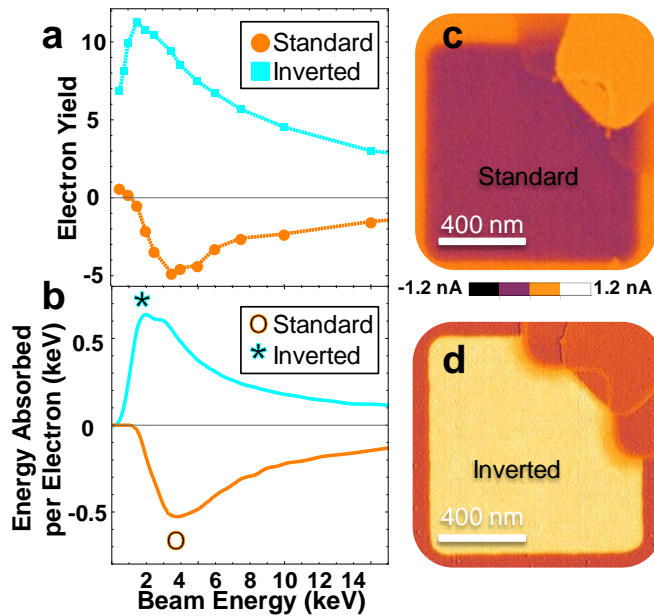

Figure 4. Pristine device measurements. a) Measured energy dependence of the electron beam induced current (EBIC) signal for the virgin device in standard and inverted devices. The measured current is

negative in the standard device and positive in inverted device. The change in sign when flipping the device over is due to reversal of the built-in field. Error bars, reflecting two standard deviations of the mean, are smaller than the markers and are determined from an area of at least 50×50 pixel bounding box on each pad. b) Monte Carlo simulation results of inverted and standard structure absorbed energy per electron. Standard structure simulation result is shown with negative sign since absorbed energy is not a negative quantity and current direction is determined by structure. c) 5 keV EBIC image of a standard device. d) 2 keV EBIC image of an inverted device. The strong similarity between the measured and simulated curves show the strong relationship between absorbed energy and generated EBIC current.
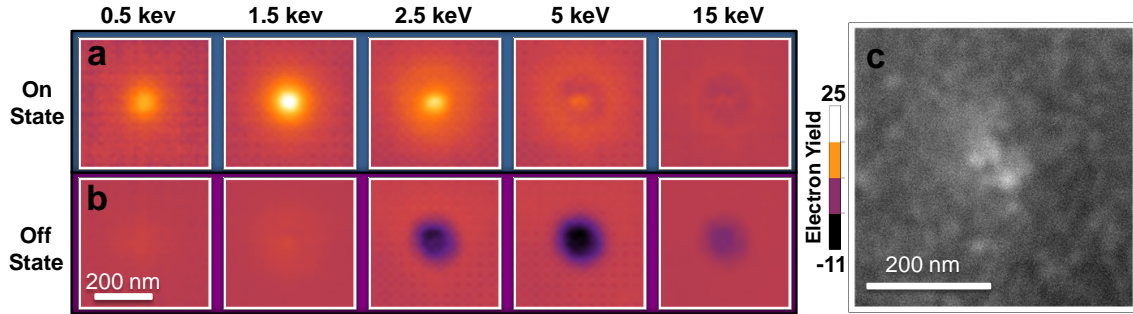

Figure 5. Micrographs of filament. a) Electron beam induced current micrograph series showing contrast evolution with beam energy for the on-state and b) for the off-state. The on-state signal maximum implies the signal is due to absorption in the top electrode whereas the the off-state signal minimum implies the signal is due to absorption in the TiO_2 layer. c) Scanning electron micrograph of the device after switching showing no tears in the electrode.
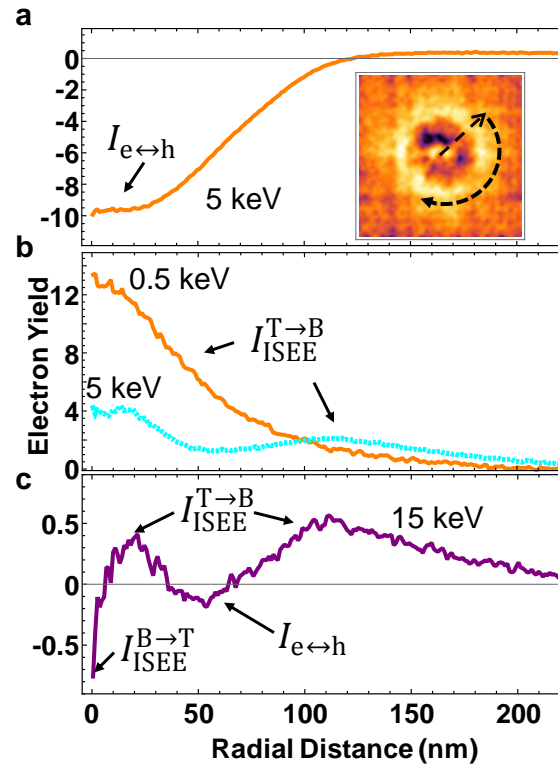

Figure 6. Radial distributions of EBIC. a) Radial plot of the azimuthally averaged electron beam induced current (EBIC) electron yield for a device in the off-state measured at 5 keV with the current mostly attributed to electron-hole pair separation and (inset) pictorial depiction of azimuthal averaging of an EBIC map. b) Radial plot of the EBIC electron yield in the on-state at low energy (0.5 keV) and an intermediate energy (5 keV) showing a signal dominated by ISEE from top to bottom but with an increasing contribution

from the other currents. c) Radial plot in the EBIC electron yield in the on-state at 15 keV showing different regions with different dominant currents (indicated by current label and arrows) leading to a radially oscillating EBIC profile.
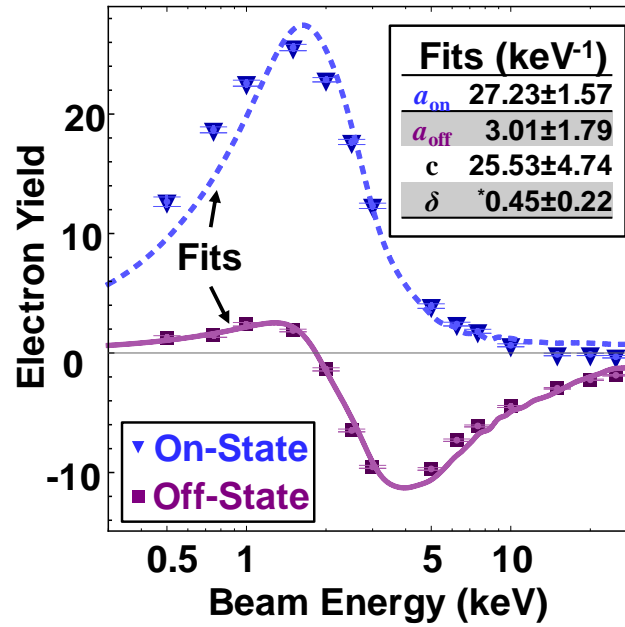

Figure 7. Experimental fit of beam energy dependence. Measured electron yield as a function of energy. Error bars indicate two standard deviations of the mean within an 11×11 pixel box at the signal center for the on-state and off-state micrograph series in Figure 5. All quantities are measured with respect to the background. Fits are shown with least-squares 95 % confidence intervals with units of keV^{-1}(*note δ is dimensionless). Only the least-squares coefficient for the internal secondary electron emission (ISEE) signal, *a*, with associated variables a_{on} and a_{off} changes between the off-state and the on-state.
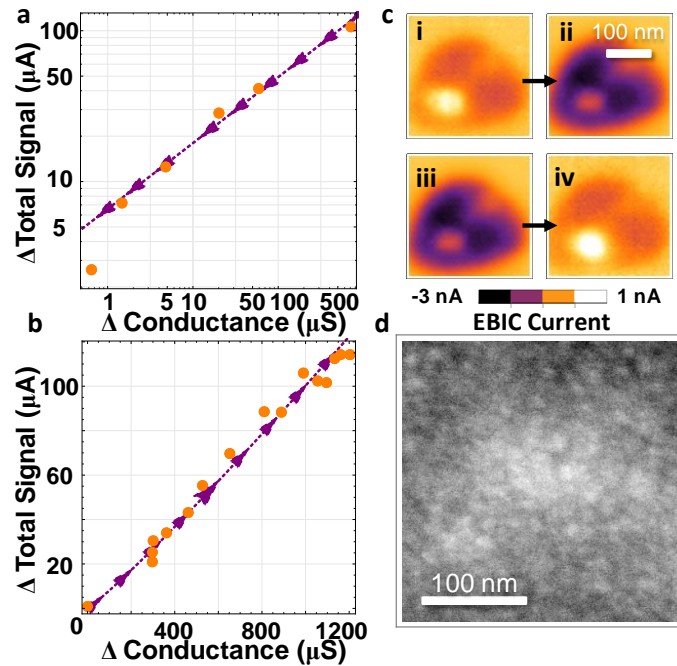
Figure 8. Conductance signal relationships. a) Comparison of the change in conductance measured at 0.1 V from the off state (ΔConductance) and the measured change in total signal in an image (ΔTotal Signal). Scaling dependence of the total electron beam induced current (EBIC) signal at 5 keV in turn-off branch with sublinear exponent 0.43±0.15 (95 % confidence). b) Scaling dependence of total EBIC signal in turn-on branch with near linear exponent 1.10±0.10 (95 % confidence), c)EBIC depiction of an on (i) to of (ii) and off(iii) to on (iv) transition. A compilation of switching micrographs for this process is available in Supplementary Movie 1. d) scanning electron microscopy image after switching showing no tearing of the electrode.
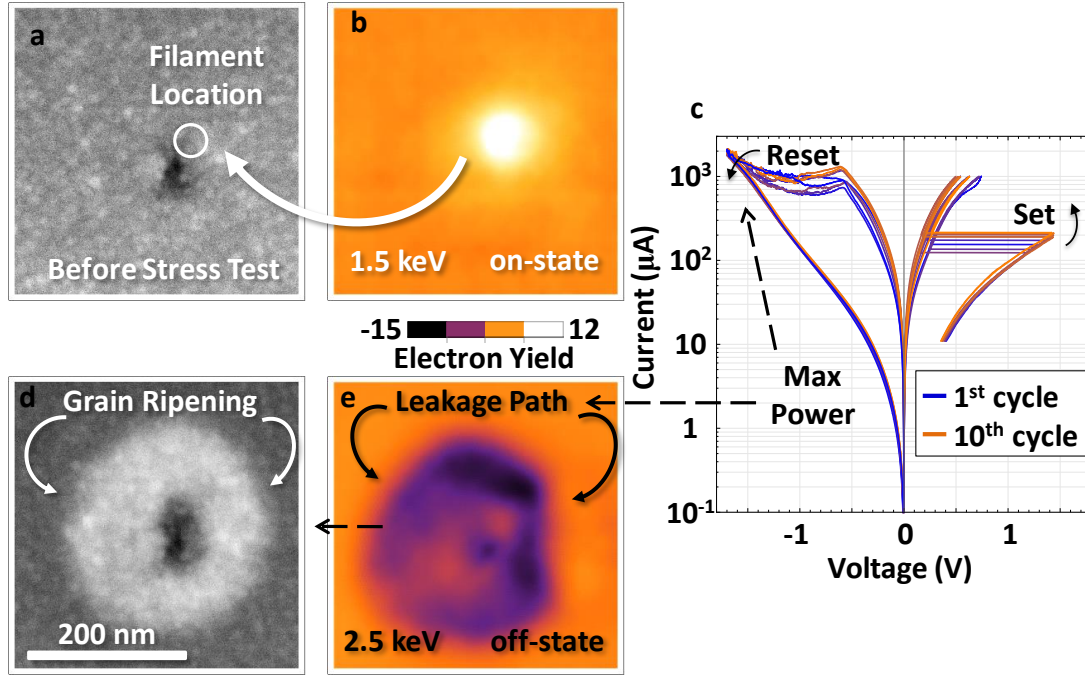
Figure 9. Stress Testing of Device. a) Scanning electron micrograph of an asymmetric standard device after forming and switching. Area adjacent to the filament is damaged by the switching. b) Electron beam induced current (EBIC) image of the device in the on-state with a low 1.5 keV beam energy. c) depiction of a 10 switching curve stress test taken after image "a". d) Scanning electron micrograph and e) corresponding EBIC image showing correspondence between grain coarsening (seen in d) and background crystallization region (region of negative current in e).
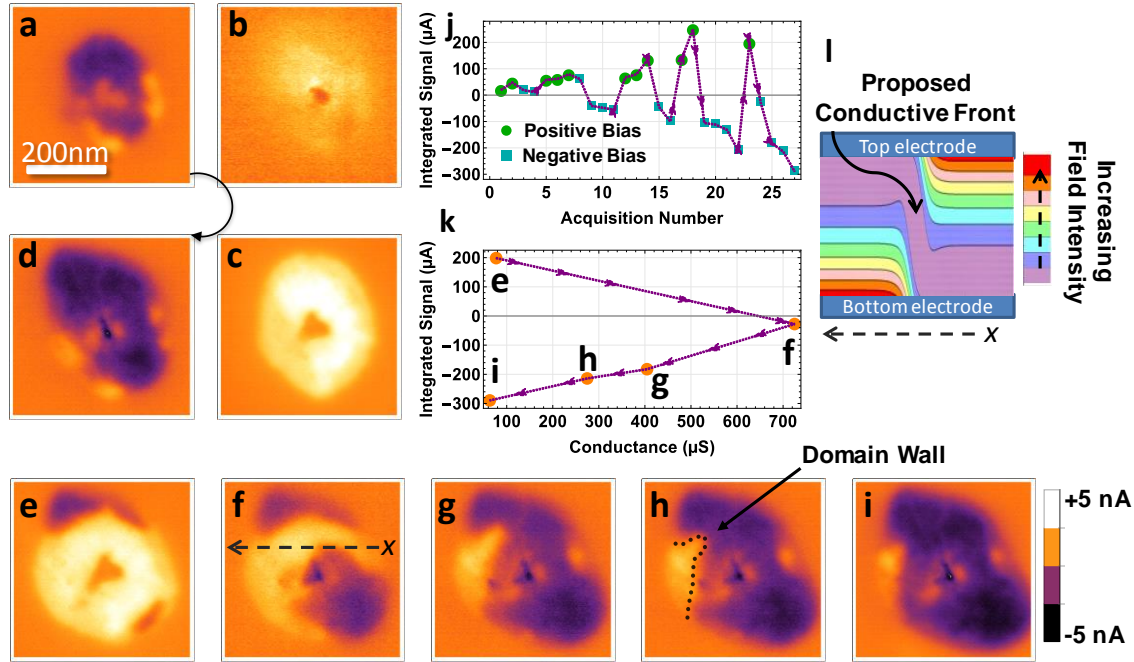
Figure 10. Reversible electron-hole signals in symmetric device. a-d) 5 keV electron beam induced current (EBIC) images of alternating hard changes in polarization observed in symmetric devices. The sign of the measured current is changing since the device built-in field is changing direction as a consequence of programming. e-i) Gradual movement of a domain wall around a barrier to encompass the entire switching region. j) Plot of effect of programming bias on device polarization with increasing amplitude of bias. k) Relationship between total EBIC signal and conductance (at 0.1 V) from stepwise transition from e to i. l) Cartoon depiction of the polarization domains with a reversal in field concentration from the top electrode to the bottom electrode with distance.